Economic Geology

BULLETIN OF THE SOCIETY OF ECONOMIC GEOLOGISTS

VOL. 104 November 2009 NO. 7

EXPRESS LETTER

*UNCLOAKING INVISIBLE GOLD: USE OF NANOSIMS TO EVALUATE GOLD, TRACE ELEMENTS, AND SULFUR ISOTOPES IN PYRITE FROM CARLIN-TYPE GOLD DEPOSITS***

SHAUN L.L. BARKER,[1,†] KENNETH A. HICKEY,[1] JEAN S. CLINE,[2] GREGORY M. DIPPLE,[1] MATT R. KILBURN,[3]
JEREMY R. VAUGHAN,[1] AND ANTHONY A. LONGO[2]

[1]*Mineral Deposit Research Unit, Department of Earth and Ocean Sciences, University of British Columbia,*
Vancouver, Canada BC V6T1Z4

[2]*Department of Geoscience, University of Nevada Las Vegas, 4505 Maryland Parkway, Box 454010, Las Vegas, Nevada 89154-4010*

[3]*Centre for Microscopy, Characterisation and Analysis M010, University of Western Australia,*
35 Stirling Highway, Crawley, WA 6009, Australia

Abstract

One-hundred-nm-resolution secondary ionizing mass spectrometry (nanoSIMS) was used to determine the distribution of Au, Cu, As, Sb, and S, and stable isotopes of S ($^{34}S/^{32}S$) in gold-bearing pyrite from two refractory Carlin-type gold deposits: West Banshee, northern Carlin Trend, and Turquoise Ridge, Getchell Trend, located in northern Nevada. NanoSIMS maps reveal that gold occurs in two discrete episodes in each deposit. Elevated gold concentrations correlate with elevated concentrations of As, Sb, Cu ± Te, and lower $^{34}S/^{32}S$ ratios, compared to periods when gold was not deposited. Precipitation of elevated gold and trace elements at West Banshee was followed by precipitation of pyrite with lower gold concentrations, whereas at Turquoise Ridge precipitation of trace element-rich pyrite was followed by precipitation of late ore-stage minerals. These NanoSIMS results are consistent with formation of the deposits by the episodic incursion of gold-rich fluids into hydrothermal systems otherwise dominated by gold-poor fluids. Such gold-rich fluid pulses may be related to incursions of magmatic fluid, which have been shown to have high concentrations of gold, arsenic, and copper in porphyry and high-sulfidation epithermal systems.

Introduction

Studies of gold-bearing hydrothermal systems typically use proxies such as fluid inclusions in, or isotopic analyses of, gangue minerals to determine the origin of the fluids in order to infer the source of gold or other metals (Ulrich et al., 1999, Harris and Golding, 2002). Refractory gold is occluded by other minerals, and where not able to be identified by optical microscopy or scanning electron microscopy is termed "invisible" gold (Cook and Chryssoulis, 1990). In contrast to studies utilizing analyses of gangue minerals spatially associated with ore minerals, analyses of the host minerals that contain invisible gold provide information on the chemical characteristics of the parent hydrothermal fluid responsible for gold precipitation. However, host minerals for invisible gold are commonly very fine grained (<1–5 μm), and previous attempts to relate refractory gold to other chemical proxies in gold-bearing minerals have been hampered by analytical techniques that lack sufficient spatial resolution and/or analytical sensitivity (Arehart et al., 1993; Kesler et al., 2003a). Here we use submicron-scale secondary ionizing mass spectrometry (nanoSIMS) to determine the distribution of Au, Cu, As, Te, S, and S isotopes ($^{34}S/^{32}S$) in gold-bearing pyrite from Turquoise Ridge and West Banshee, two Carlin-type gold deposits in Nevada. Clear patterns of chemical zoning in the pyrite grains provide insights into the genesis of these enigmatic gold deposits.

Previous Studies and Geologic Setting

The world-class Carlin-type gold deposits of northern Nevada provide 9 percent of global gold production (Cline et al., 2005; Price et al., 2008). Most of the gold is disseminated in deposits within silty carbonate host rocks that were decarbonatized during hydrothermal alteration (Cline et al., 2005). The upper, supergene oxidized portions of the deposits contain

---

[†] Corresponding author: e-mail, sbarker@eos.ubc.ca

**A digital supplement for this paper is available at <http://www.geoscienceworld.org/> or, for subscribers, on the SEG website, <http://subscriptions.segweb.org/>.

©2009 by *Economic Geology*, Vol. 104, pp. 897–904
0361-0128/09/3844/897-8

Submitted: August 26, 2009
Accepted: October 2, 2009

free gold and were the focus of initial exploration and development (Bettles, 2002). Subsequent exploration and mining delineated bodies of refractory gold that is submicroscopic in fine-grained Fe sulfide minerals, primarily pyrite (Wells and Mullens, 1973; Arehart et al., 1993; Simon et al., 1999). Ore-stage pyrite is believed to form via sulfidation of preexisting Fe silicate and Fe carbonate minerals, and bisulfide-complexed metals including gold were adsorbed on and incorporated in the precipitating pyrite (Hofstra et al., 1991; Kesler et al., 2003a). Debate continues over the sources of fluid (meteoric, magmatic, or metamorphic) and metal (upper crust black shales, magmatic, or mantle) in the Carlin systems, and whether mineralization occurred in single or multiple events (see Muntean et al., 2004; Cline et al., 2005). Rocks in northern Nevada have been affected by several hydrothermal events, ranging in age from Devonian to Miocene (Hofstra et al., 1999; Emsbo et al., 2003; Cline et al., 2005), making recognition of the key characteristics of the main Carlin gold-forming hydrothermal event difficult to distinguish. Thus, the distribution of gold in ore-stage pyrite and spatial relationships of gold with other elements provide an opportunity to examine the compositional evolution of the Carlin-type ore-stage hydrothermal fluid.

Several studies have used various analytical techniques to study pyrite in Carlin-type deposits, including electron probe microanalysis (EPMA; Wells and Mullens, 1973; Cline and Hofstra, 2000; Hofstra and Cline, 2000; Cline, 2001; Cline et al., 2003a; Emsbo et al., 2003; Henkelman, 2004; Reich et al., 2005) and secondary ionizing mass spectrometry (SIMS; Arehart et al., 1993; Simon et al., 1999; Cline, 2001; Kesler et al., 2003a; Palenik et al., 2004; Reich et al., 2005) to quantify gold and a suite of associated elements including As, Sb, Hg, Tl, Cu, and Te that occur in refractory pyrite. Trace element-rich pyrite occurs typically as thin rims (<10 μm) on pyrite formed prior to Carlin mineralization or as tiny discrete spherical grains (<5 μm). Within trace element-rich pyrite, transmission electron microscopy (TEM) and high resolution TEM (HRTEM) have shown that gold is both structurally bound (Au^1) and also occurs as free gold (Au^0) nanoparticles (Bakken et al., 1989; Simon et al., 1999; Palenik et al., 2004; Reich et al., 2005).

Pyrite grains from three representative samples of high-grade Carlin-type ore were analyzed in this study. The first is a sample of lamprophyre dike (49 ppm Au; sample H07-13b-476; Figs. 1, 2) from the West Banshee deposit located in the northern Carlin Trend, 2.5 km northwest of the giant Betze-Post deposit (~40 million ounces (Moz) Au; Bettles, 2002). Mineralization is focused in a lamprophyre dike and surrounding breccia body. The sample contains (1) abundant trace element-poor pyrite, (2) As- and Au-enriched pyrite that occurs as both tiny spheroidal grains and rims on the earlier trace element poor pyrite grains, and (3) arsenopyrite, all set in a groundmass of quartz and illite. This particular dike has not been dated directly, but all similar lamprophyre dikes that have been dated on the northern Carlin Trend have an age of ~158 Ma (Emsbo et al., 1996; Ressel and Henry, 2006). The other two samples are from the Turquoise Ridge deposit, which is located near the Getchell deposit on the Getchell Trend (>6.6 Moz Au, Chevillon et al., 2000). Sample 936 881 consists of decalcified and silicified tuffaceous mudstone and limestone from the High Grade Bullion ore zone (161 ppm Au; Fig. 3). Sample 664 211 consists of highly deformed and decalcified tuffaceous mudstone and limestone and clasts of preore quartz from the 148 ore zone (64 ppm Au; Fig. 4). Both samples contain preore pyrite cores rimmed by trace element-rich pyrite and tiny spherical trace element-rich pyrites that generally do not exhibit preore cores.

Methods

Pyrite grains in the samples chosen for analysis were characterized using optical and backscattered electron (BSE) scanning microscopy, and EPMA. NanoSIMS analysis was carried out on selected pyrite grains, with maps characterizing both complete grains and sections of grains from core to rim.

Electron probe microanalysis (EPMA) was carried out in the Geoscience Department, University of Nevada Las Vegas, using a JEOL JXA-model 8900 instrument. A 2-μm electron beam at 20-kV accelerating voltage and 10-nA current was used for determination of Fe, S, and As, and 100-nA current for determination of other trace element concentrations. While EPMA has quantified ore pyrite chemistry and delineated distinct chemical zones across some ore-stage rims in these deposits (Cline et al., 2003b; Longo et al., 2008, 2009) the 2-μm electron beam and larger excitation volume partially homogenizes the sub micrometer-scale chemical zoning of the rims revealed by nanoSIMS analysis.

Elemental and isotopic mapping were performed using the Cameca NanoSIMS 50 at the University of Western Australia. Samples were polished and coated with Pt or C for conductivity at high voltage. For element mapping a focused 1- to 2-pA Cs^+ primary ion beam was rastered across the sample surface recording images from the secondary ions (depending on the analytical routine) ^{32}S, ^{63}Cu, ^{75}As, $^{197}Au \pm {}^{121}Sb \pm {}^{126}Te$, simultaneously. In some samples, analyses recorded images from secondary ions $^{63}Cu^{32}S$ and $^{75}As^{32}S$ to provide improved count rates. Areas ranging from 60 × 60 to 15 × 15 μm were imaged at a pixel resolution of 256 × 256, with a primary beam diameter of approximately 100 nm. Peaks were calibrated using chalcopyrite (Cu), arsenopyrite (As), PbTe, and metallic Au. Images of ^{195}Pt were also obtained to ensure that there was no contribution to ^{197}Au from $^{196}Pt^1H$ in the Pt coat. The isotope ^{126}Te was chosen to eliminate potential interferences from Sn, Sb, and I.

Isotope measurements were obtained by producing secondary ion images of $^{32}S^-$ and $^{34}S^-$ simultaneously. Stacks of 14 or 20 individual images were recorded sequentially over 8 or 12 h, respectively. These stacks were aligned, summed, and corrected for detector deadtime and quasisimultaneous arrival effects (Slodzian et al., 2004). Sulfur isotope maps show relative ratios across pyrite grains, but are semiquantitative in nature, as sulfur isotope standards that would allow sulfur isotope ratios to be compared to results from previous studies were not analyzed.

Results

The submicron resolution of nanoSIMS images reveals that the pyrites have systematic zoning of Au, Cu, As, Sb, Te, and S (Figs. 1A-B, 2, 3, Table 1). Sulfur isotope ratio ($^{34}S/^{32}S$) maps (Figs. 1C, 4) allow direct comparison of changes in

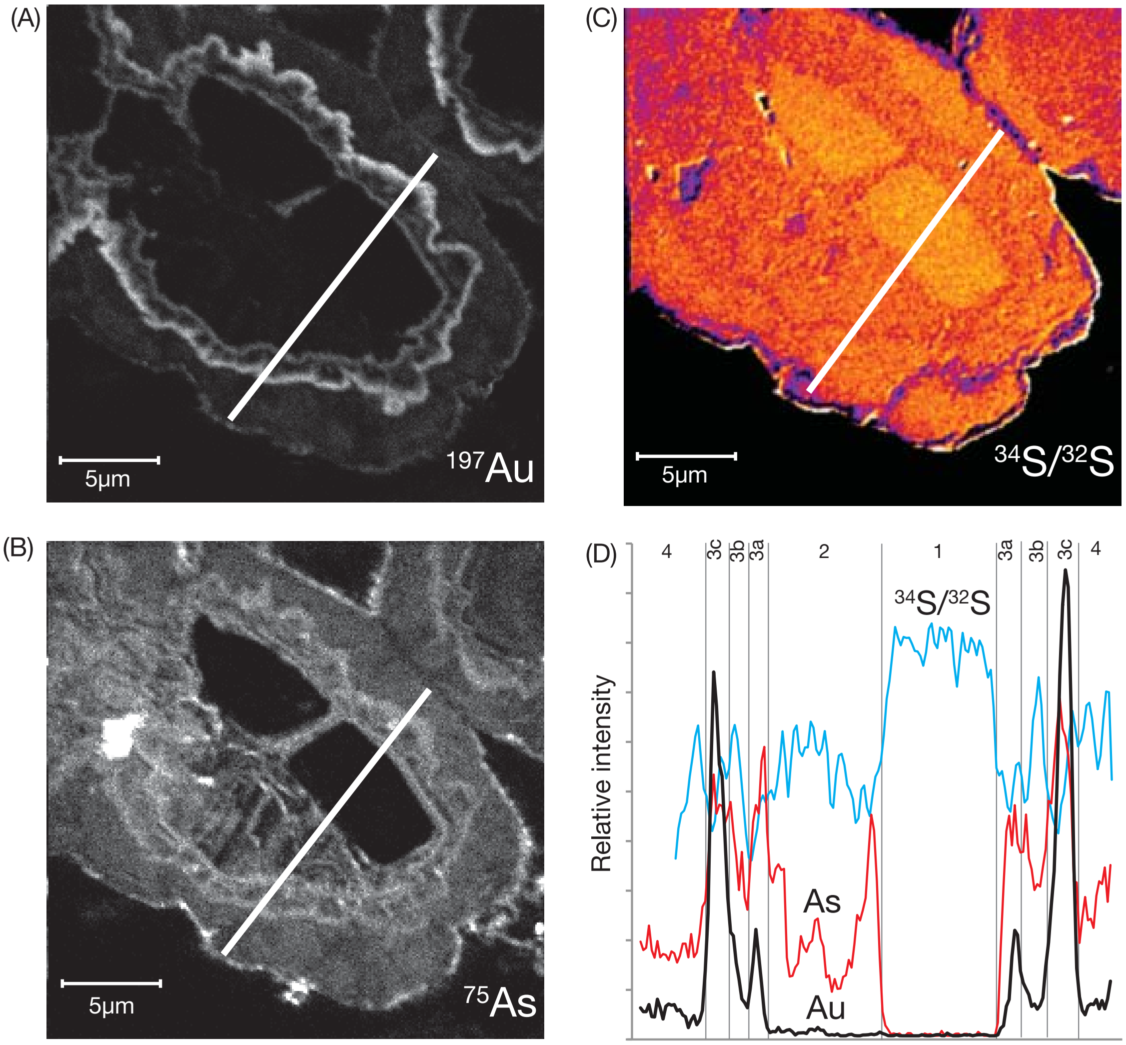

FIG. 1. NanoSIMS maps of ore-stage pyrite from the West Banshee deposit: (A) distribution of gold (lighter grays are higher Au concentrations), (B) arsenic (lighter grays are higher As concentrations), and (C) sulfur isotope ratios ($^{34}S/^{32}S$, hotter colors are higher $^{34}S/^{32}S$ ratios) in ore-stage pyrite from the West Banshee deposit. (D) Relative intensity profiles of Au (black line), As (red line), and $^{34}S/^{32}S$ (blue line) along lines in maps shown in (A) to (C). Four growth stages can be distinguished based on mineral chemistry and texture. Stage 1 is characterized by below detection Au and low As concentrations and higher $^{34}S/^{32}S$ ratios, stage 2 has higher As concentrations, below detection Au and lower $^{34}S/^{32}S$, stages 3a to 3c have variably elevated Au and As concentrations, and the lowest $^{34}S/^{32}S$ ratios, and represent the Carlin gold event. Stage 4 has lower Au and As concentrations than stage 3, and higher $^{34}S/^{32}S$ ratios. The high relief and irregular morphology of Au-rich growth stage 3c implies growth at higher pyrite supersaturation. For further description of growth stages and associated changes in trace element compositions, please see the text.

trace element concentrations with relative changes in sulfur isotope ratios for pyrite containing invisible gold. Here, we use growth stages to define chemical and morphological zones within pyrite grains. We note that distinct growth stages are defined independently for each deposit and do not imply any temporal relationship.

West Banshee

Large pyrite grains (>5 μm) analyzed from the West Banshee deposit preserve evidence of four growth stages (Fig. 1). Stage 1 in the core of the grains is characterized by gold values below detectable limits (<90 ppm, see Table 1, Fig 1A), low As concentrations (<0.1% wt, Fig. 1B), higher $^{34}S/^{32}S$ relative to the rest of the grain (Fig. 1C), and planar growth boundaries (Fig. 1). Stage 2 has elevated As (~ 4% wt), below detection Au concentrations, lower $^{34}S/^{32}S$ relative to stage 1 and irregular growth boundaries (Fig. 1, Table 1). Growth stage 3 is characterized by elevated Au concentrations between 220 and 890 ppm (Table 1) and represents the ore stage of pyrite growth in the West Banshee samples. Stage 3 has two thin (~0.5 μm) Au-rich zones (stages 3a and 3c) separated by a slightly wider zone (0.5–1.0 μm) of lower Au (stage 3b; Fig. 1A). The gold-rich rims 3a and 3c have different morphologies; 3a directly mimics the irregular shape of the stage 2 boundary, whereas 3c has a more irregular, higher relief growth boundary (Fig. 1A). NanoSIMS maps and EPMA indicate that growth stage 3 in all pyrite grains has elevated concentrations of Au, Cu (Fig. 2; Table 1), Hg,

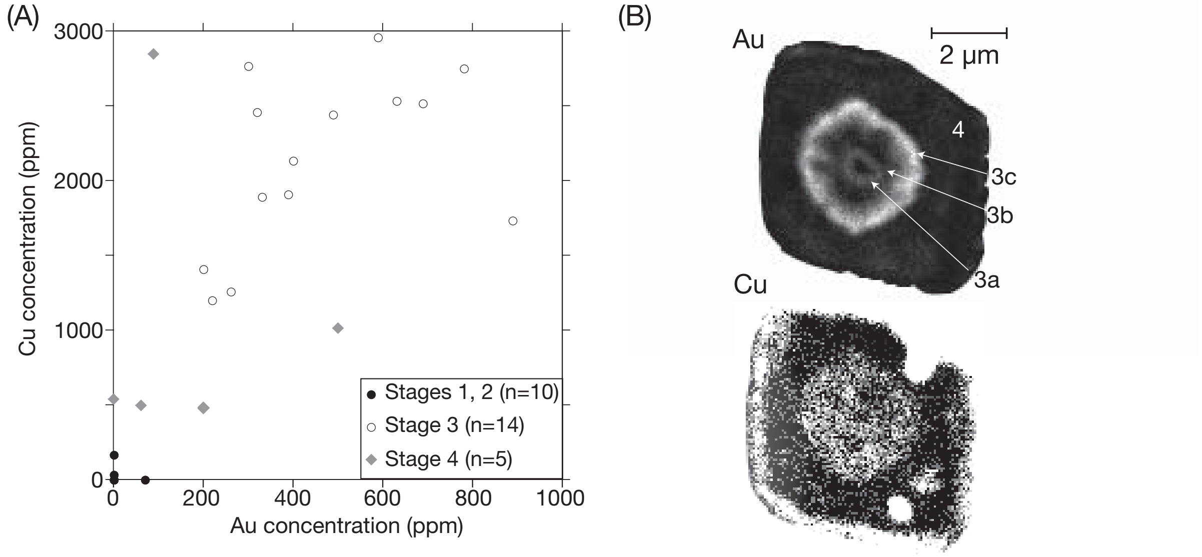

FIG. 2. (A). Results from electron microprobe analyses from pyrite growth stages 1 to 4 from West Banshee (see supplementary data set for all analyses). Note that growth stage 3 has the most elevated gold and copper concentrations. (B). Au and Cu maps showing the distribution of gold and copper within tiny (~5 μm) ore-stage pyrite. Note correlation between Cu- and Au-rich cores of these pyrite grains.

As, and Sb. Sulfur isotope maps have a low signal/noise ratio in the West Banshee samples, making it difficult to distinguish stage 3 of pyrite growth. However, in the line profiles of ^{34}S/^{32}S (Fig. 1D), growth stages 3a and 3c are coincident with subtly lower ^{34}S/^{32}S values (Fig. 1C). Stage 4 of pyrite growth (Fig. 1A) has slightly elevated gold concentrations compared to stages 1 and 2 and lower concentrations of Au, Cu, Hg, As, and Sb compared to stage 3 (Table 1). This outermost stage has a more regular, lower relief growth boundary than stages 2 and 3. Analysis of the nanoSIMS images from the West Banshee deposit suggests that stage 3 contains between 70 and 85 percent of total gold within each of the pyrite grains, with stage 4 accounting for most of the remaining gold. Small (<5 μm), near-equant pyrite grains are ubiquitous in the West Banshee deposit. At West Banshee, these small pyrite grains contain significant gold concentrations (260–640 ppm Au) and are characterized by a gold-rich central region corresponding to stages 3a, b, and c in the larger grains (Fig. 2).

Turquoise Ridge

NanoSIMS images (Fig. 3) and EPMA analyses (Table 1) of pyrite grains in sample 936 881 reveal three stages of pyrite growth (Fig. 3). Stage 1 has gold concentrations below detection limits (EPMA) and low concentrations of other trace elements (see Table 1, for representative analyses, other analyses are given in the supplementary data set). Stage 2 is a thin zone characterized by slightly elevated but outwardly increasing Cu (~450 ppm) and As concentrations (~400 ppm). Stage 3 is the main ore stage of pyrite growth. It has two peaks in Au concentration (stage 3a, 1,470 ppm and 3c, 2,240 ppm) separated by a zone of lower Au values (stage 3b, 820 ppm). Arsenic closely mimics the Au peaks, having the highest concentration in stage 3c. Compared to

TABLE 1. Representative EPMA Analyses from Growth Stages 1 to 4 of Pyrites at West Banshee and Growth Stages 1 to 3 of Pyrite from Sample 936 881 at Turquoise Ridge (note that full analyses may be found online in the supplementary data set; URL information on p. 897)

Times		Ni (ppm)	Mo (ppm)	Zn (ppm)	Hg (ppm)	Au (ppm)	Ag (ppm)	Sb (ppm)	Te (ppm)	Cu (ppm)	Fe (% wt)	S (% wt)	As (% wt)	Total (% wt)
Detection limit (ppm)		163	285	176	95	91	99	112	128	210	558	1493	310	
West Banshee	Growth stages													
	Stage 1	1760	BDL	BDL	BDL	BDL	BDL	BDL	BDL	BDL	46.19	53.94	0.04	100.84
	Stage 2	5130	BDL	BDL	150	BDL	BDL	1180	BDL	BDL	43.85	49.55	4.00	99.53
	Stage 3	380	BDL	BDL	500	890	130	1940	BDL	1730	44.79	50.12	3.04	99.04
	Stage 4	BDL	BDL	BDL	BDL	BDL	BDL	140	BDL	540	44.95	51.97	2.42	99.91
Turquoise Ridge														
	Stage 1	BDL	BDL	BDL	0	BDL	BDL	BDL	BDL	650	46.01	53.38	0.01	99.72
	Stage 2	BDL	BDL	BDL	0	BDL	BDL	BDL	BDL	730	45.92	52.90	0.04	99.37
	Stage 3a	BDL	BDL	BDL	1670	1410	BDL	BDL	BDL	2100	40.90	44.11	13.17	99.03
	Stage 3b	BDL	BDL	BDL	2870	660	BDL	BDL	1860	2630	41.35	48.94	4.48	96.10
	Stage 3c	BDL	BDL	BDL	2550	1140	BDL	BDL	BDL	1930	42.30	51.12	2.55	97.49

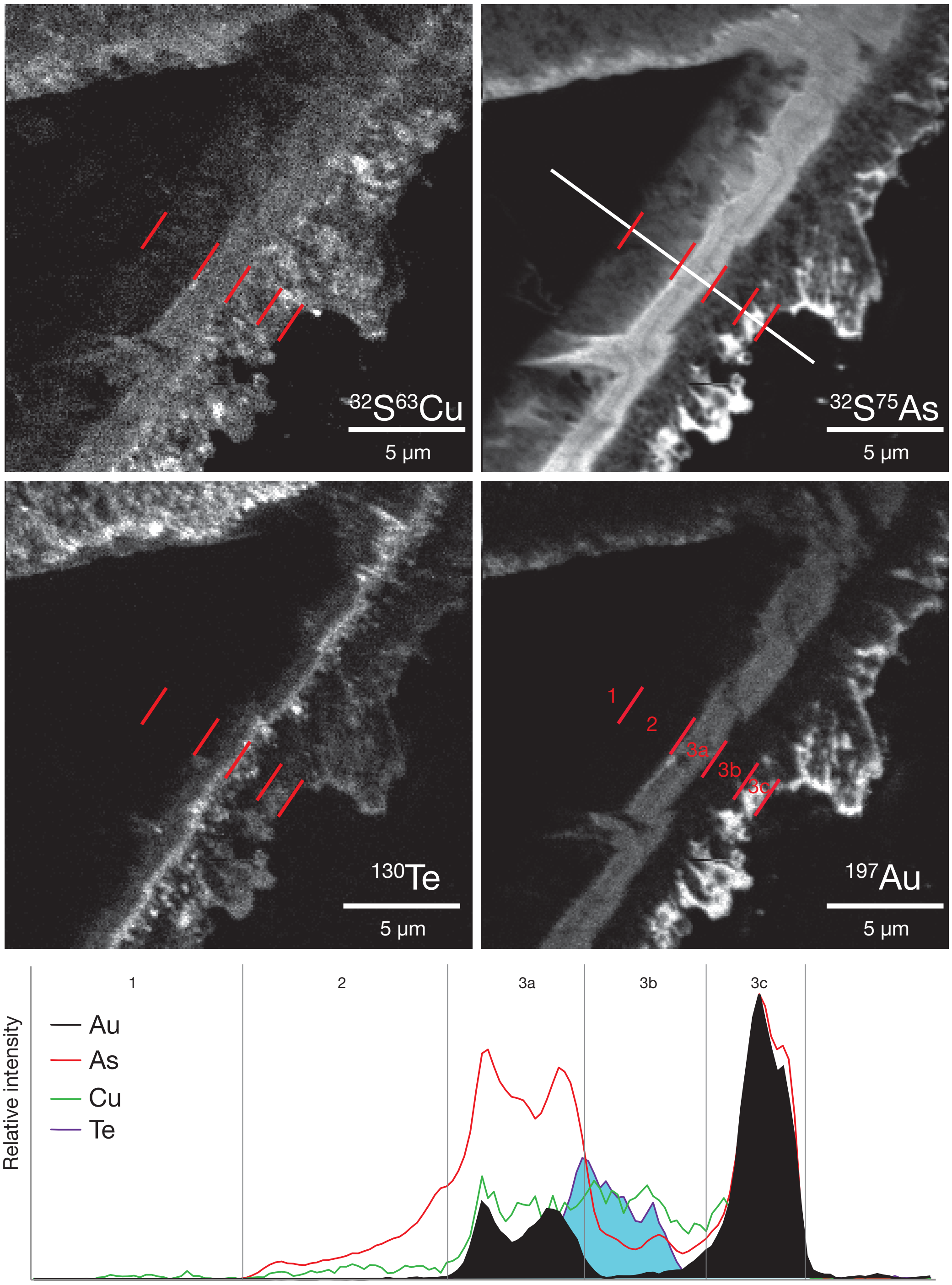

FIG. 3. Trace element maps from Turquoise Ridge pyrite grain (936 881), showing the distribution of Cu (as $^{32}S^{63}Cu$), As (as $^{32}S^{75}As$), Te (as ^{130}Te), and Au (as ^{197}Au). Different growth stages are separated by red lines in each trace element map and are labeled as growth stages 1, 2, 3a, 3b, and 3c in the Au map. Stages 3a, b, and c represent the Carlin Au event. Shown at the bottom are relative intensity profiles of Au (black line), As (red line), Te (purple line), and Cu (green line) along white line shown in the $^{32}S^{75}As$ map. Separate growth stages are labeled on the line profile.

stages 1 and 2, Cu concentrations are elevated across stage 3, decreasing slightly toward the margin of the grain, without distinct peaks that mimic those of Au (Fig. 3). Tellurium has low concentrations across stage 2 but rises steady through stage 3a, reaching a peak at the boundary of stages 3a and b. It then decreases before peaking again in stage 3c, mimicking exactly the outer peaks in As and Au (Fig. 3). Stage 3a has a regular morphology that parallels the regular outer edge of stages 1 and 2, whereas stages 3b and c have irregular, high relief growth boundaries.

In contrast to sample 936 881, sample 664 211 has a single gold-rich rim, overgrowing two earlier stages of pyrite growth.

Sulfur isotope maps of sample 664 211 illustrate that preore stage 1 has the highest $^{34}S/^{32}S$ ratios, preore stage 2 has lower $^{34}S/^{32}S$ than stage 1, and stage 3, which contains Au and other trace metals, has the lowest $^{34}S/^{32}S$ ratios (Fig. 4).

Interpretation

Observations of pyrite textures and chemical zonation have several important implications for ore-forming processes in these two Carlin-type deposits: (1) gold occurs in two discrete, thin, growth stages, implying that gold-rich pyrite growth occurred in separate, short-lived episodes at both West Banshee and Turquoise Ridge; (2) changes in pyrite growth morphology accompanying elevated gold concentrations are interpreted to be the result of higher degrees of pyrite supersaturation; (3) higher gold concentrations are accompanied by lower $^{34}S/^{32}S$ ratios (which may be related to a change in fluid source and/or fluid oxidation); and (4) differences in the relative zoning of gold and other trace elements across single pyrite grains are interpreted to represent the influx and evolution of distinct ore fluids.

We interpret the cores (stage 1) of pyrite grains at both West Banshee and stages 1 and 2 at Turquoise Ridge as representing pyrite formation that occurred prior to Carlin mineralization. Previous studies of deposits from the Carlin and Getchell Trends have demonstrated that the trace element-rich pyrites are surrounded by ore-stage quartz (Cline, 2001; Lubben et al., 2003) and/or late ore-stage hydrothermal minerals (e.g., realgar; Cline, 2001), thus we conclude that the trace element-rich pyrite formed during the Carlin hydrothermal system. Stages 3 to 4 at West Banshee and stage 3 at Turquoise Ridge are therefore interpreted as being solely products of the hydrothermal system responsible for alteration and gold deposition. A significant difference between the two deposits is that in samples from West Banshee, gold-rich stage 3 pyrite is preceded and overgrown by zones of trace element-poor pyrite (stages 2 and 4), whereas trace

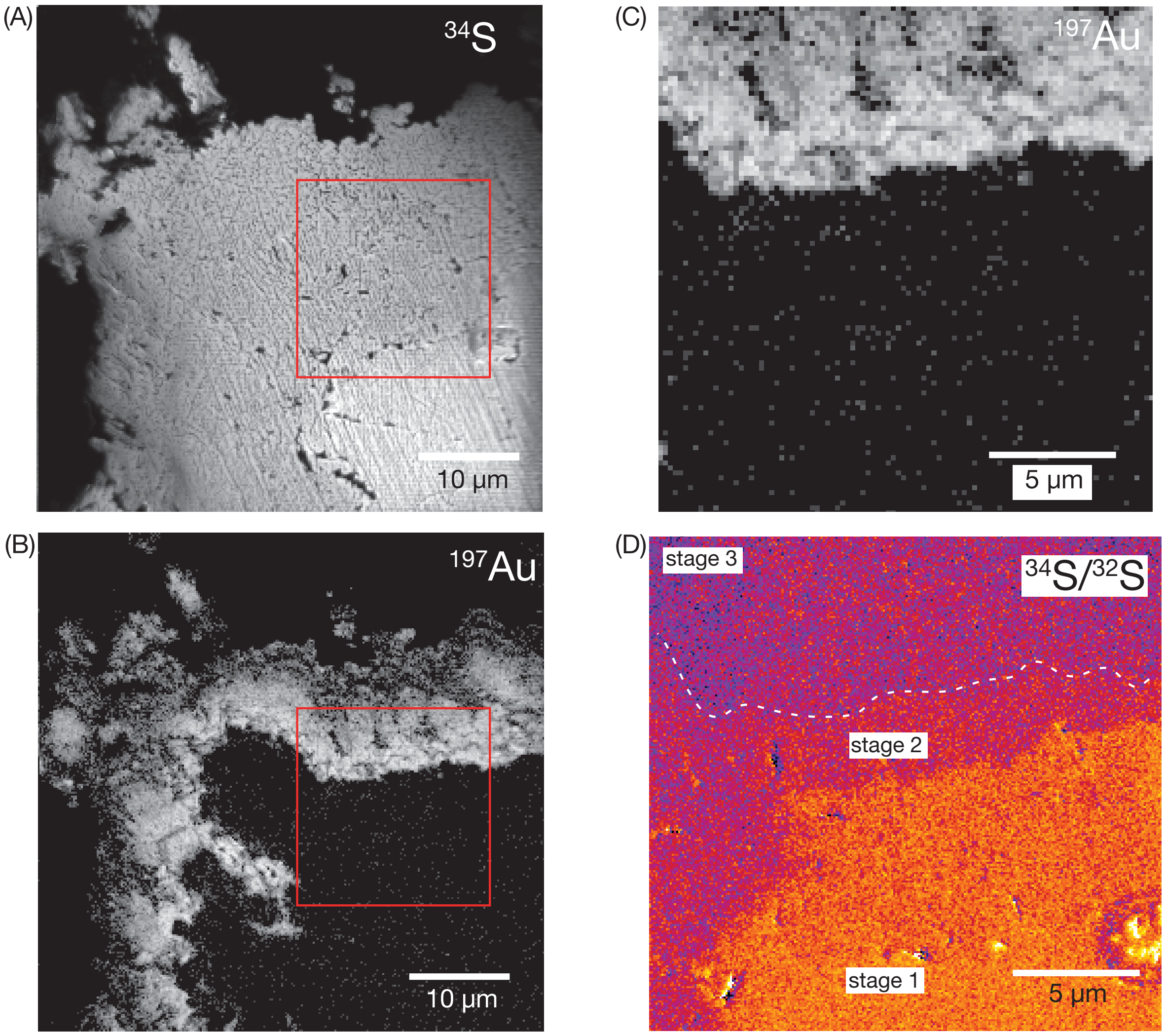

FIG. 4. NanoSIMS maps showing distribution of: (A) ^{32}S (denoting the distribution of pyrite), (B) ^{197}Au in ore-stage pyrite sample 664 211 from Turquoise Ridge, (C) ^{197}Au for the area inside the red square shown in (A) and (B). (D). Sulfur isotope ratio ($^{32}S/^{32}S$) over almost exactly the same area as the map of ^{197}Au shown in (C), with the dashed white line in (D) representing the boundary between gold-poor and gold-rich pyrite. Note the strong correlation between distribution of gold in (C) and change in sulfur isotope ratios in (D).

element-rich pyrite (stage 3) at Turquoise Ridge was instead overgrown by late ore-stage minerals including drusy quartz, orpiment, fluorite, realgar, and calcite.

In growth stages 3a and c from the West Banshee deposit, the distribution and thickness of gold-rich zones are similar on all crystal faces. This suggests that the distribution of gold in these pyrite grains was controlled by gold availability in the fluid, rather than by crystallographic structural control (Chouinard et al., 2005). These observations lead to the interpretation that stages 3a and 3c of trace element-rich pyrite at West Banshee reflect two episodes of gold enrichment related to two hydrothermal fluids with distinct trace metal ratios. At Turquoise Ridge stages 3a and 3c are defined by coincident peaks in Au and As concentration but have variable Te and only slight differences in Cu. This variation in trace element distribution likely reflects the chemical evolution of an Au-Cu-Te-As–bearing fluid during stages 3a and 3b of pyrite growth; possibly reflecting the variable breakdown of associated metal complexes and/or the rate of adsorption and incorporation into the growing pyrite.

Pyrite formation at low temperature likely occurs via supersaturation and precipitation of FeS, which is subsequently converted to pyrite via reaction with aqueous sulfide and sulfur to form FeS_2 (Rickard, 1975). Irregular grain shapes of stages 2 to 4 at West Banshee and stage 3 at Turquoise Ridge suggest Fe sulfide precipitation during supersaturated conditions (Murowchick and Barnes, 1987). The most irregular growth boundaries are characterized by the highest gold concentrations, suggesting that a single process caused Fe sulfide supersaturation and precipitation and provided the highest concentrations of gold.

Sulfur isotope compositions of sulfide minerals provide information about the source, transport, and precipitation mechanisms of sulfur (Ohmoto and Goldhaber, 1997). The correlation of higher gold concentrations with the lowest $^{34}S/^{32}S$ values in pyrite precipitated as part of the Carlin hydrothermal system at West Banshee (Fig. 1) and Turquoise Ridge (Fig. 4) suggests that gold incorporation into pyrite was linked to the influx of a fluid with a distinct sulfur isotope composition, or that gold incorporation into pyrite was linked to an event that caused fractionation of sulfur isotopes (e.g., fluid oxidation). Further analytical work is required to evaluate these possibilities.

Implications and Conclusions

Conventional SIMS and EPMA studies of refractory pyrite are often hampered by large sampling volumes relative to the size of gold-bearing pyrite (Arehart et al., 1993; Kesler et al., 2003a). NanoSIMS reveals the relative distribution of gold, other trace elements, and sulfur isotopes within ore-stage pyrite in refractory gold deposits and has sufficient spatial resolution to reveal zoning patterns that have important implications for the genesis of hydrothermal mineral deposits.

At both West Banshee and Turquoise Ridge, gold-rich pyrite rims have elevated concentrations of trace elements that also include As, Sb, Hg, Cu, and Te. NanoSIMS images clearly reveal a metal suite that accompanied Au in the ore fluid and precipitated in pyrite with Au. These images further demonstrate the presence of two temporally and chemically distinct ore-stage fluid pulses at West Banshee. At Turquoise Ridge the Au and As profiles also suggest the influx of two distinct pulses of ore-stage fluids. However, the inconsistent correlation of Au and As with Cu and Te suggests some additional controls on the rates at which these metals were incorporated into pyrite as it precipitated.

Previous EPMA analyses (Wells and Mullens, 1973; Hofstra and Cline, 2000; Cline, 2001; Emsbo et al., 2003; Henkelman, 2004) and analyses that are part of this study demonstrate that pyrite with elevated gold concentrations does not have elevated concentrations of Ni, Mo, or Zn compared to other pyrite growth stages (see Table 1); whereas, these elements do have elevated concentrations in many preore pyrite cores (Cline, 2001; Henkelman, 2004) and in diagenetic pyrite associated with SEDEX gold mineralization in the northern Carlin Trend (Large et al., 2009), suggesting that gold- and trace element-rich pyrite in stage 3 is not related to SEDEX mineralization.

At both the West Banshee and Turquoise Ridge deposits, pyrite growth persisted between the two intervals when elevated gold and other trace metals were incorporated into pyrite. At West Banshee, latest stage 4, low gold pyrite, is also present. These observations indicate that Fe availability and the sulfidation process, both thought to be key to the formation of Carlin deposits, persisted when no or little gold was incorporated into pyrite. Based on these observations we infer that pulses of exotic gold- and trace element-rich fluid were added to a hydrothermal system, which otherwise precipitated gold- and trace element-poor pyrite. At West Banshee, the hydrothermal system continued to grow pyrite after the final pulse of gold-rich fluid, whereas at Turquoise Ridge, the final stage of gold-rich pyrite precipitation was followed by the precipitation of realgar and other late ore-stage hydrothermal minerals.

Ore-stage pyrite is thought to have precipitated as acidic ore fluids that reacted with and decalcified silty pyritic carbonate rocks, exposing reactive Fe (Hofstra et al., 1991; Hofstra and Cline, 2000; Cline et al., 2005). Low fluid pH facilitated both decalcification and liberation of Fe and increased Au adsorption (Widler and Seward, 2002), and gold grade and pyrite abundance may, therefore, in part be related to fluid pH. The presence of two chemically distinct ore-stage Au rims at both West Banshee and Turquoise Ridge, as illustrated by nanoSIMS images, suggests the input of two discrete packages of ore fluid at both deposits. The chemistry of the two fluids may have varied owing to chemical variations in fluid source or perhaps related to variations in conditions at the site of precipitation such as varying pH, which could have affected the amount of trace metals adsorbed on the precipitating pyrites.

Fluid and metal sources for these deposits have not been identified, but fluid metal ratios indicated by EPMA of pyrites and delineated in much greater detail by nanoSIMS analyses are very similar to metal ratios in high-sulfidation epithermal systems (Kesler et al., 2003b). This metal suite could have been generated by immiscibility of an exsolving aqueous fluid from a deep calc-alkaline magma, which would have partitioned bisulfide-complexed metals including Au to an aqueous vapor, separating them from chloride-complexed Fe and base metals that would partition to the liquid (Heinrich, 2005). Thus the metal suites identified by EPMA and nanoSIMS in Carlin deposits are consistent with suites produced by magmatic processes in porphyry and high-sulfidation epithermal deposits.

Acknowledgments

MDRU would like to thank Teck, Barrick Gold Corp., and Newmont Mining Corp., through NSERC-CRD grant CRDP J 355066-07, for logistical and financial support throughout this study. In particular, the authors would like to thank C. Weakly for arranging access to the Banshee deposit and B. Leonardson for very helpful comments on a draft manuscript. J.S. Cline acknowledges NSF grant 0635658 and thanks Barrick Gold Corp. and Placer Dome Exploration for project support. The authors thank Mike Hochella and Jeff Hedenquist for their very thorough reviews of this paper and Larry Meinert for editorial guidance. This is MDRU publication no. 254.

REFERENCES

Arehart, G.B., Chryssoulis, S.L., and Kesler, S.E., 1993, Gold and arsenic in iron sulfides from sediment-hosted disseminated gold deposits: Implications for depositional processes: Economic Geology v. 88, p. 171–185.

Bakken, B.M., Hochella, M.F., Jr., Marshall, A.F., and Turner, A.M., 1989, High-resolution microscopy of gold in unoxidized ore from the Carlin mine, Nevada: Economic Geology, v. 84, p. 171–179.

Bettles, K. 2002, Exploration and geology, 1962–2002 at the Goldstrike property, Carlin Trend, Nevada: Economic Geology Special Publication 9, p. 275–298.

Chevillon, V., Berentsen, E., Gingrich, M., Howla, D.B., and Zbinden, E., 2000, Geological overview of the Getchell gold mine geology, eexporation, and ore deposits, Humboldt County, Nevada. Geology and gold deposits of the Getchell Trend: Society of Economic Geologists Guidebook Series, v. 32, p. 195–201.

Chouinard, A., Paquette, J., and William-Jones, A.E., 2005, Crystallographic controls on trace-element incorporation in auriferous pyrite from the Pascua epithermal high-sulfidation deposit, Chile-Argentina: Canadian Mineralogist, v. 43, p. 951–963.

Cline, J.S., 2001, Timing of gold and arsenic sulfide mineral deposition at the Getchell Carlin-type gold deposit, north-central Nevada: Economic Geology, v. 96, p. 75–89.

Cline, J.S., and Hofstra, A.H., 2000, Ore fluid evolution at the Getchell Carlin-type gold deposit, Nevada, USA: European Journal of Mineralogy, v. 12, p. 195–212.

Cline, J.S., Stuart, F.M., Hofstra, A.H., Premo, W., Riciputi, L., Tosdal, R.M., and Tretbar, D., 2003a, Multiple sources of ore-fluid components at the Getchell Carlin-type gold deposit, Nevada, USA: Mineral Exploration and Sustainable Development, Seventh Biennial SGA Meeting, Athens, Greece, Proceedings, p. 965–968.

Cline, J.S., Shields, D., Riciputi, L., Fayek, M., Copp, T., Muntean, J., and Hofstra, A.H., 2003b, Trace element and isotope microanalyses support a deep ore fluid source at the Getchell Carlin-type gold deposit, northern Nevada [abs.]: Geological Society of America Abstracts with Programs, v. 35, p. 358.

Cline, J.S., Hofstra, A.H., Muntean, J.L., Tosdal, R.M., and Hickey, K.A., 2005, Carlin-type gold deposits in Nevada: Critical geological characteristics and viable models: Economic Geology 100th Anniversary Volume, p. 451–484.

Cook, N.J., and Chryssoulis, S.L., 1990, Concentrations of “invisible gold” in the common sulfides: Canadian Mineralogist, v. 28, p. 1–16.

Emsbo, P., Hofstra, A.H., Park, D., Zimmerman, J.M., and Snee, L., 1996, A mid-Tertiary age constraint on alteration and mineralization in igneous dikes on the Goldstrike property, Carlin Trend, Nevada [abs.]. Geological Society of America Abstracts with Programs, v. 28, A476.

Emsbo, P. Hofstra, A.H., Lauha, E.A., Griffin, G.L., and Hutchinson, R.W., 2003, Origin of high-grade gold ore, source of ore fluid components, and genesis of the Meikle and neighboring Carlin-type deposits, northern Carlin Trend, Nevada: Economic Geology, v. 98, p. 1069–1105.

Harris, A.C., and Golding, S.D., 2002, New evidence of magmatic-fluid-related phyllic alteration: Implications for the genesis of porphyry Cu deposits: Geology v. 30, p. 335–338.

Heinrich, C.A., 2005, The physical and chemical evolution of low-salinity magmatic fluids at the porphyry to epithermal transition: A thermodynamic study: Mineralium Deposita, v. 39, p. 864–889.

Henkelman, C., 2004, Variations in pyrite chemistry as clues to gold deposition at the Goldstrike system, Carlin Trend, Nevada, USA: Unpublished M.Sc. thesis, Las Vegas, University of Nevada, 150 p.

Hofstra, A.H., and Cline, J.S., 2000, Characteristics and models for Carlin-type gold deposits: Society of Economic Geologists Reviews, v. 13, p. 163–220.

Hofstra, A.H., Leventhal, J.S., Northrop, H.R., Landis, G.P., Rye, R.O., Birak, D.J., and Dahl, A.R., 1991, Genesis of sediment-hosted disseminated-gold deposits by fluid mixing and sulfidization: Chemical-reaction-path modeling of ore-depositional processes documented in the Jerritt Canyon district, Nevada: Geology, v. 19, p. 36–40.

Hofstra, A.H., Snee, L.W., Rye, R.O., Folger, H.W., Phinisey, J.D., Loranger, R.J., Dahl, A.R., Naeser, C.W., Stein, H.J., and Lewchuk, M.T., 1999, Age constraints on Jerritt Canyon and other Carlin-type gold deposits in the Western United States—relationship to Mid-Tertiary extension and magmatism: Economic Geology, v. 94, p. 769–802.

Kesler, S.E., Fortuna, J., Ye, Z., Alt, J.C., Core, D.P., Zohar, P., Borhauer, J., and Chryssoulis, S.L., 2003a, Evaluation of the role of sulfidation in deposition of gold, Screamer section of the Betze-Post Carlin-type deposit, Nevada: Economic Geology, v. 98, p. 1137–1157.

Kesler, S.E., Ye, Z., Fortuna, J., and Riciputi, L.C., 2003b, Epithermal–Carlin transition: Evidence for magmatic input into Carlin-type deposits, *in* Eliopoulos, D.G., ed., Mineral exploration and sustainable development: Rotterdam, Millpress, p. 493–494.

Large, R., Danyushevsky, L., Hollit, C., Maslennikov, V., Meffre, S., Gilbert, S., Bull, S., Scott, R., Emsbo, P., Thomas, H., Singh, B., and Foster, J., 2009, Gold and trace element zonation in pyrite using a laser imaging technique: Implications for the timing of gold in orogenic and Carlin-style sediment hosted deposits: Economic Geology v. 104, p. 635–668.

Longo, A.A., Cline, J.S., and Muntean, J., 2008, Compositional variations in Au-bearing pyrite from a Carlin-type Au deposit, Getchell, Nevada [abs.]: Geological Society of America Abstracts with Programs, v. 40, no. 1, p. 51.

——2009, Detecting ore fluid pathways in Carlin-type gold deposits using pyrite chemistry [abs.]: Society for Geology Applied to Mineral Deposits, Abstracts with Program, Townsville, Australia.

Lubben, J.D., Cline, J.S., and Fairhurst, R.J., 2003, Cathodoluminescence in quartz: Clues to ore paragenesis and ore fluid properties at the Goldstrike Carlin-type gold deposit, northern Nevada [abs.]: Geological Society of America Abstracts with Programs, v. 35, p. 267

Muntean, J.L., Cline, J., Johnston, M.K., Ressel, M.W., Seedorf, E., and Barton, M.D., 2004, Controversies on the origin of world-class gold deposits. Part I: Carlin-type gold deposits in Nevada: Society of Economic Geologists Newsletter, v. 59, p. 11–18.

Murowchick, J.B., and Barnes, H.L., 1987, Effects of temperature and degree of supersaturation on pyrite morphology: American Mineralogist, v. 72, p. 1241–1250.

Ohmoto, H., and Goldhaber, M., 1997, Sulfur and carbon isotopes, *in* Barnes, H.L., ed., Geochemistry of hydrothermal ore deposits, 3rd ed.: New York, Wiley, p. 517–611.

Palenik, C.S., Utsonomiya, S., Reich, M., Kesler, S.E., and Wang, L., 2004, “Invisible” gold revealed: Direct imaging of gold nanoparticles in a Carlin-type deposit: American Mineralogist, v. 89, p. 1359–1366.

Price, J.G. et al., 2008, The Nevada Minerals Industry 2007: Nevada Bureau of Mines and Geology Special Publication MI-2007.

Reich, M., Kesler, S.E., Utsunomiya, S., Palenik, C.S., Chryssoulis, S.L., and Ewing, R.C., 2005, Solubility of gold in arsenian pyrite: Geochimica et Cosmochimica Acta, v. 69, p. 2781–2796.

Ressel, M.W., and Henry, C.D., 2006, Igneous geology of the Carlin Trend, Nevada: Development of the Eocene plutonic complex and significance for Carlin-type gold deposits: Economic Geology, v. 101, p. 347–383.

Rickard, D.T., 1975, Kinetics and mechanism of pyrite formation at low temperatures: American Journal of Science, v. 275, p. 636–652.

Simon, G., Kesler, S.E., and Chryssoulis, S., 1999, Geochemistry and textures of gold-bearing arsenian pyrite, Twin Creeks, Nevada: Implications for the deposition of gold in Carlin-type deposits: Economic Geology, v. 94, p. 405–421.

Slodzian, G., Hillion, F., Stadermann, F.J., and Ziner, E., 2004, QSA influences on isotopic ratio measurements: Applied Surface Science, v. 321–323, p. 874–877.

Ulrich, T., Gunther, D., and Heinrich, C.A., 1999, Gold concentrations of magmatic brines and the metal budget of porphyry copper deposits: Nature, v. 399, p. 676–679.

Wells, J.D., and Mullens, T.E., 1973, Gold-bearing arsenian pyrite determined by microprobe analysis, Cortez and Carlin gold mines, Nevada: Economic Geology, v. 68, p. 187–201.

Widler, A.M., and Seward, T.M., 2002, The adsorption of gold (I) hydrosulphide complexes by iron sulphide surfaces: Geochimica et Cosmochimica Acta, v. 66, p. 383–402.